



Electrocatalytic reduction of nitrate to ammonia on low-cost manganese-incorporated Co_3O_4 nanotubes

Di Liu^{a,1}, Lulu Qiao^{a,1}, Yuyun Chen^a, Pengfei Zhou^a, Jinxian Feng^a, Chon Chio Leong^b, Kar Wei Ng^{a,c}, Shengjie Peng^d, Shuangpeng Wang^{a,c,*}, Weng Fai Ip^c, Hui Pan^{a,c,*}

^a Institute of Applied Physics and Materials Engineering, University of Macau, Macau

^b Department of Electrical and computer Engineering, Faculty of Science and Technology, University of Macau, Macau

^c Department of Physics and Chemistry, Faculty of Science and Technology, University of Macau, Macau

^d College of Materials Science and Technology, Nanjing University of Aeronautics and Astronautics, Nanjing 210016 China

ARTICLE INFO

Keywords:

Ammonia yield
Electrocatalytic nitrate reduction reaction
Spinel Co_3O_4
Mn incorporation
DFT calculations

ABSTRACT

Spinel oxides, especially Co_3O_4 , have been considered as ideal electrocatalysts for electrocatalytic nitrate reduction reaction (e- NO_3RR). However, their application in e- NO_3RR is still limited because of relatively low activity and selectivity under high potential. Herein, we present that the incorporation of manganese (Mn) into the Co_3O_4 lattice can achieve the high activity and selectivity in e- NO_3RR . The Mn-incorporated Co_3O_4 nanotubes show a remarkable e- NO_3RR activity with a high ammonia yield rate of $35 \text{ mg h}^{-1} \text{ cm}^{-2}$ and excellent selectivity with a Faraday efficiency for ammonia up to 99.5% in neutral media, which are much better than those of transition-metal oxides. Our calculations further show that the replacement of Co by Mn can tune the adsorption behavior of intermediates, and thus reduces the limiting potential of e- NO_3RR . We believe that the findings provide an insightful guidance to engineer the spinel oxides for enhanced performance towards ideal products.

1. Introduction

The worldwide demand for ammonia has been growing with the development of society since 1950 s because of its essentiality in modern agriculture and industry [1]. Currently, the production of ammonia heavily depends on the Haber-Bosch process, which needs to be carried out under high temperature and pressure [2–5], consumes large amount of natural gas [6], and leads to serious energy and environmental issues. As one of alternative ways, the electrocatalytic nitrogen reduction reaction (e-NRR) has been explored extensively over the years [6–16]. However, extensive efforts are needed because of very poor Faraday efficiency and low yield rates. The inferior performance is induced not only by the high dissociation energy of $\text{N}\equiv\text{N}$ bond (941 kJ mol^{-1}), but also by the poor N_2 solubility in water under ambient conditions due to its non-polar nature [17–21]. In addition, e-NRR occurs at the gas-liquid-solid interface, which dynamically hinders the performance too [13,22–24].

Compared with e-NRR, the electrocatalytic reduction of nitrate anion (electrocatalytic nitrate reduction reaction (e- NO_3RR)) is much practical

to be industrialized due to the relatively low dissociation energy of $\text{N}=\text{O}$ bond, the high solubility of nitrate in aquatic environment and the fast dynamic process at the liquid-solid interface [25–29]. At the same time, NO_3^- as an environmental pollutant is widely present in low-level nuclear wastewater, industrial wastewater, and polluted ground water [4]. Thus, the e- NO_3RR process not only provides a green way for ammonia synthesis, but addresses the environmental pollution [4,30]. Importantly, the over-all cost of ammonia synthesized by e- NO_3RR is similar to that of the Haber-Bosch process, which is promising for its application in industry [4,31]. However, the reduction towards nitrogen by a 5-electron process, other than to ammonia by an 8-electron process, is also possible during the reduction of nitrate [31–33]. Additionally, the production of hydrogen is inevitable during e- NO_3RR because of the duplicate reduction potential with electrocatalytic hydrogen evolution reaction (e-HER) [34]. Though various catalytic systems, including metals, alloys, and compounds, have been applied in e- NO_3RR , they tend to convert NO_3^- to N_2 rather than to the desired ammonia [32,33,35, 36]. Therefore, the selectivity towards ideal ammonia needs to be improved [4]. Progress on the improvement of selectivity and activity

* Corresponding authors at: Institute of Applied Physics and Materials Engineering, University of Macau, Macau.

E-mail addresses: spwang@um.edu.mo (S. Wang), huipan@um.edu.mo (H. Pan).

¹ [†] These authors contributed equally to this work.

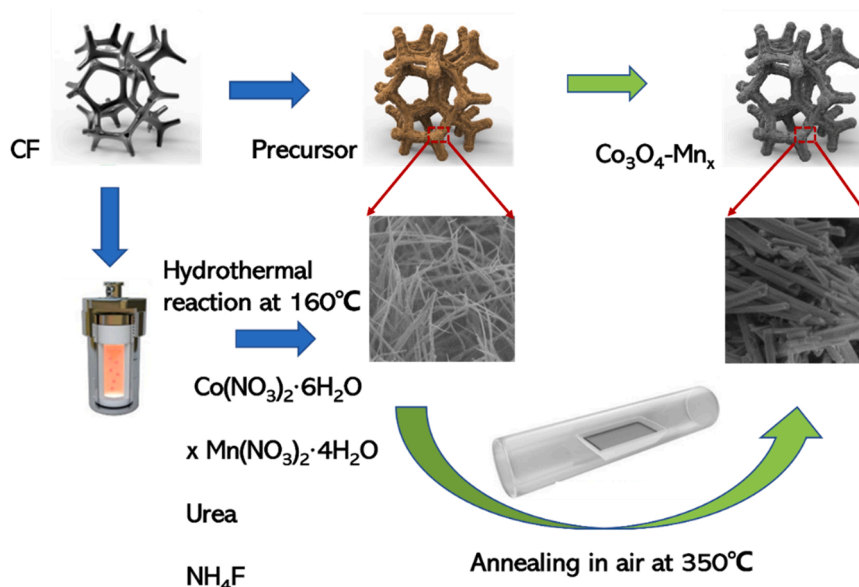


Fig. 1. Scheme for the synthesis of $\text{Co}_3\text{O}_4\text{-Mn}_x$ nanotubes.

has been reported using noble-metal-based materials [37–39]. However, the industrial application in e- NO_3RR is still difficult to be realized due to their high cost and rare reserves. Therefore, searching electrocatalysts with the high cost-to-price ratio is urgent for the ammonia production, where transition metal-based materials, including oxides, carbides, and phosphides [40–49], have been extensively explored. Importantly, these explorations provide insightful understanding and general strategies, such as introduction of vacancies, optimization of electronic structure, improvement of electron accumulation and depletion, and chemical-environment modulation, to improve the catalytic activity and selectivity for ambient ammonia yield [13,14,45–52], which have been demonstrated to be effective for e- NO_3RR [45–48,53,54]. Although they showed high efficiency for the ammonia production, it is hard to fabricate them on large scale in industry, or keep them stable for long-term application, which inhibits their commercial utilization. Recently, spinel oxides have attracted increasing attention for their applications as electrocatalysts in e- NO_3RR because of their good stability and easy fabrication, which may be applicable to industries [55–59]. For example, Co_3O_4 has shown a Faraday efficiency (FE) up to 93.4% at -0.3 V vs. reversible hydrogen electrode (RHE) in e- NO_3RR [55]. However, the ammonia partial current density of Co_3O_4 is still too low to be practical, which cannot be improved by applying high voltage because FE is reduced accordingly. At the same time, as spinel Co_3O_4 consists of CoO_4 tetrahedrons and CoO_6 octahedrons, the origin for its e- NO_3RR activity is still under debate [60]. To reveal the underlying mechanism of Co_3O_4 -based materials and further improve the catalytic performance, various strategies have been explored, such as the replacement of Co ions in CoO_4 and CoO_6 by inactive transition metal elements, and the introduction of cobalt / oxygen vacancies [60–65], which could modify the electronic structure, inhabit the competitive HER, and improve the catalytic performance [60,61,63–67]. Though these works provided insightful understandings and reported the highest ammonia yield of $17.52 \text{ mg h}^{-1} \text{ cm}^{-2}$, further improvement on the ammonia yield is still needed for practical applications [60,61,63–67].

Here, we propose that the Mn-incorporation can improve the ammonia yield rate and selectivity of Co_3O_4 dramatically and provide a platform to reveal the mechanism. The Mn-incorporated Co_3O_4 was fabricated by a simple hydrothermal + annealing method and used for the reduction of nitrate to ammonia. By systematically studying the effect of Mn/Co ratio, we find that the Mn/Co of 2:1 ($\text{Co}_3\text{O}_4\text{-Mn}_2$) leads to the highest ammonia yield rate of $35 \text{ mg h}^{-1} \text{ cm}^{-2}$ and high FE up to more than 99.5% at -1.2 V vs RHE under ambient condition and neutral

pH value, which outperforms most of reported catalysts for e- NO_3RR . Especially, compared with these reported Co_3O_4 -based catalysts, the $\text{Co}_3\text{O}_4\text{-Mn}_2$ sample possesses much higher ammonia yield rate.

2. Experimental section

2.1. Synthesis of $\text{Co}_3\text{O}_4\text{-Mn}_x$ nanotubes

$\text{Co}_3\text{O}_4\text{-Mn}_x$ nanotubes were fabricated on a commercial cobalt foam (CF) by using a hydro-thermal reaction + annealing method. Firstly, a piece of CF ($6 \text{ cm} \times 10 \text{ cm} \times 0.2 \text{ mm}$) was ultrasonically cleaned in deionized (DI) water and ethanol solution for several times and dried under ambient condition. Subsequently, the foam was immersed in autoclave with solution consisting of $x \text{ mmol Co(NO}_3)_2 \cdot 4 \text{ H}_2\text{O}$, $(1.5-x) \text{ mmol Co(NO}_3)_2 \cdot 4 \text{ H}_2\text{O}$, $2 \text{ mmol Co(NH}_2)_2$, 30 ml DI water , and $1 \text{ mmol ammonium fluoride}$. Then, the autoclave was heated to 120°C , and kept for 8 h . The obtained precursor was washed by DI water for several times and dried under ambient condition. After that, the precursor was placed in a tube furnace, heated to 350°C , and kept for 2 h . Then, the $\text{Co}_3\text{O}_4\text{-Mn}_x$ nanotubes were obtained. For the materials characterizations, the powders were collected by ultrasonication for avoiding the influence of substrate.

2.2. Characterizations

Field emission scanning electron microscopy (FE-SEM) images were acquired on a Zeiss Sigma instrument at the acceleration voltages of 2 and 15 kV , respectively. X-ray diffraction (XRD) data were obtained on a Rigaku Smartlab X-ray diffractometer with $\text{Cu K}\alpha$ radiation ($\lambda = 0.15406 \text{ nm}$). High-resolution transmission electron microscopy (HRTEM) and energy-dispersive X-ray spectra analysis (EDX) were performed on a Tecnai G2F30 system at an acceleration voltage of 200 kV . The X-ray photoelectron spectroscopy (XPS) was obtained on a Thermo Fisher Scientific Theta Probe with $\text{Mg K}\alpha$ ($h\nu = 1253.6 \text{ eV}$) as the excitation source. The Raman measurements were performed on a Horiba LABHRV-UV System. All Ultraviolet-visible (UV-Vis) absorption spectra experiments were implemented on the Shimadzu UV-2600 spectrophotometer (Tokyo, Japan). The generated ammonia was verified by an isotope-labelled tracer experiment using $0.1 \text{ M } ^{15}\text{NO}_3^-$ as the N source. After 1 h of electroreduction at -1.0 V , the electrolyte ($50 \mu\text{L}$) was mixed with Deuterium oxide (D_2O , $500 \mu\text{L}$), which was sealed into a nuclear magnetic resonance (NMR) tube (5 mm in diameter, 600 MHz)

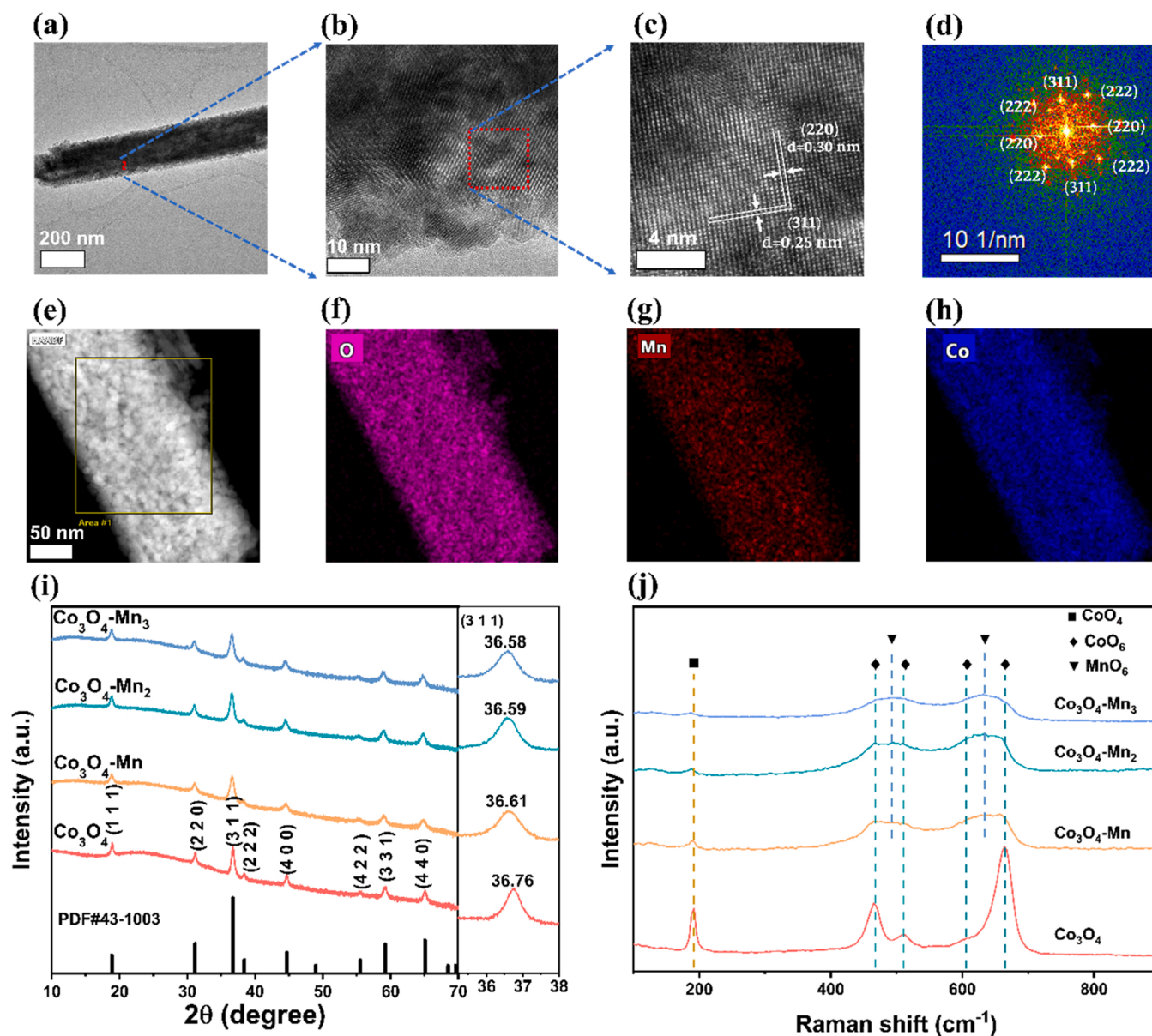


Fig. 2. $\text{Co}_3\text{O}_4\text{-Mn}_x$ nanotubes: (a) TEM image, (b) & (c) HRTEM image, (d) FFT image, (e) HAADF-STEM image, and the elemental EDX mappings for (f) O, (g) Mn, and (h) Co. (i) XRD patterns of $\text{Co}_3\text{O}_4\text{-Mn}_x$ (inset is the fine view for the (311) peak). (j) Raman spectra of $\text{Co}_3\text{O}_4\text{-Mn}_x$.

for further test. The Faradaic efficiency of H_2 was measured by gas chromatography (7890B; Agilent Technologies) with a thermal conductivity detector (TCD). The working electrode area was 0.4 cm^2 .

2.3. Electrochemical measurements

Electrochemical measurements were carried out on a ModuLab XM workstation at ambient condition. An H-type electrochemical cell with a Celgard 2500 membrane as a separator was employed in all experiments. The membrane was fully washed with DI water prior to use. The prepared $\text{Co}_3\text{O}_4\text{-Mn}_x$ (the geometric area: $0.5 \text{ cm} \times 0.8 \text{ cm}$) and Co_3O_4 with the same area were used as working electrode, respectively. A Pt foil and Ag/AgCl electrode (saturated KCl) were used as the counter and reference electrodes, respectively. The two compartments of H-cell were filled with 40 ml solution ($0.5 \text{ M K}_2\text{SO}_4 + 0.1 \text{ M KNO}_3$), respectively, and then degassed by Ar (99.999%) for more than 30 mins. The polarization curves were recorded by linear sweep voltammetry (LSV) at a scan rate of 10 mV s^{-1} without iR correction from -0.3 to -2 V vs. Ag/AgCl. Furthermore, for investigating the Faraday efficiency and yield

rate of NH_3 , the chronoamperometry (i-t) was performed at different potentials for 1 h. The chronoamperometry (i-t) was performed at different potentials for 0.5 h for low nitrate concentrations. The current density was obtained by normalizing with the geometric area of the working electrode if not specially clarified. All recorded electrode potentials vs. Ag/AgCl were transformed to potentials against RHE according to $E_{\text{RHE}} = E_{\text{Ag/AgCl}} + 0.197 + 0.0591 \times \text{pH}$. Electrochemical impedance spectroscopy (EIS) was recorded in a frequency range of 10 kHz to 0.01 Hz at the amplitude of 10 mV. The electrochemically active surface area (ECSA) was estimated by measuring the double-layer capacitance (C_{dl}) via the CV test at the scan rates of $40\text{--}100 \text{ mV s}^{-1}$.

3. Results and discussion

3.1. Synthesis and characterization

The samples were prepared using $\text{Mn}(\text{NO}_3)_2 \cdot 4 \text{ H}_2\text{O}$ and $\text{Co}(\text{NO}_3)_2 \cdot 6 \text{ H}_2\text{O}$ as solution, where the Mn-to-Co ratio was controlled to be 0:1, 1:1, 2:1 and 3:1 (labeled as Co_3O_4 , $\text{Co}_3\text{O}_4\text{-Mn}$, $\text{Co}_3\text{O}_4\text{-Mn}_2$ and $\text{Co}_3\text{O}_4\text{-Mn}_3$,

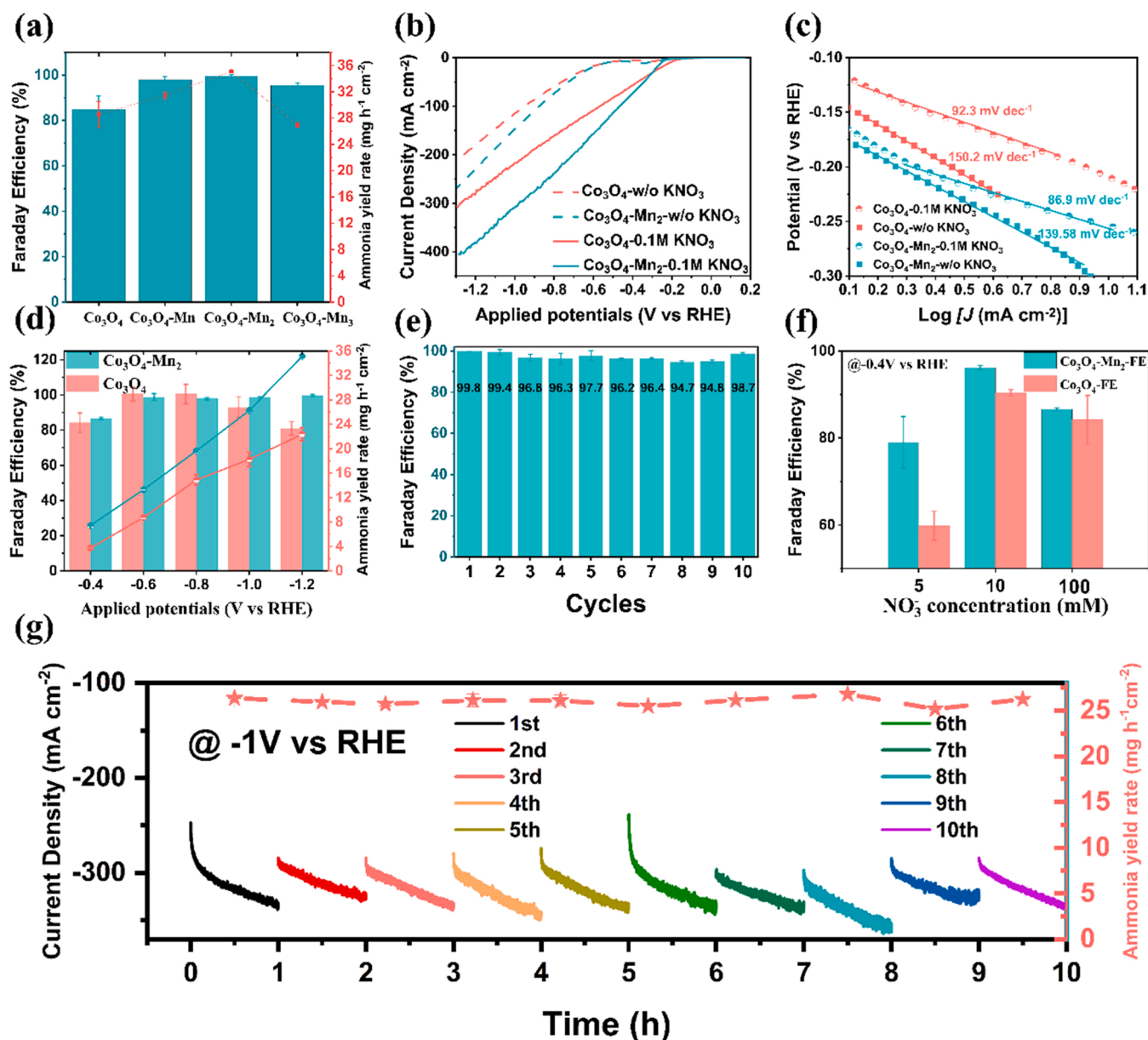


Fig. 3. Electrocatalytic performances of $\text{Co}_3\text{O}_4\text{-Mn}_x$. (a) ammonia yield and FE under -1.2 V vs. RHE in the $0.5 \text{ M K}_2\text{SO}_4 + 0.1 \text{ M KNO}_3$ solution; (b) LSV curves of Co_3O_4 (red) and $\text{Co}_3\text{O}_4\text{-Mn}_2$ (blue) measured in Ar-saturated $0.5 \text{ M K}_2\text{SO}_4$ (dash lines) and $0.5 \text{ M K}_2\text{SO}_4 + 0.1 \text{ M KNO}_3$ (straight lines), and (c) corresponding Tafel plots; (d) ammonia yield and FE at different potentials for e- NO_3RR ; (e) ammonia FEs for $\text{Co}_3\text{O}_4\text{-Mn}_2$ during the durability test (number in %: FE of each cycle); (f) ammonia FEs for Co_3O_4 and $\text{Co}_3\text{O}_4\text{-Mn}_2$ at -0.4 V versus RHE in electrolytes with different nitrate concentrations; and (g) I-t curves and ammonia yield of $\text{Co}_3\text{O}_4\text{-Mn}_2$ during the durability test.

respectively) (Fig. 1). The SEM images show that Co_3O_4 , $\text{Co}_3\text{O}_4\text{-Mn}$, $\text{Co}_3\text{O}_4\text{-Mn}_2$ are nanotubes, while $\text{Co}_3\text{O}_4\text{-Mn}_3$ is composed of nanowires and nanoplates (Figs. S1 and S2). The TEM result confirms the nanotube structure that has a diameter in the range of 50–100 nm (Fig. 2a and S3). The high-resolution TEM (HRTEM) and Fast Fourier transfer (FFT) show that the lattice spacings of 0.25 and 0.29 nm are the Co_3O_4 (220) and Co_3O_4 (311) facets, respectively, which agree well with the spinel Co_3O_4 lattice and are in accordance with the selected area electron diffraction (SAED) image (Fig. 2b–2d, S3a & S4a). The high-angle annular dark-field scanning TEM image (HAADF-STEM) and the corresponding elemental EDX mappings confirm the existence of Co, Mn, and O elements, and the calculated Mn-Co ratio in $\text{Co}_3\text{O}_4\text{-Mn}_2$ is about 1:3 (Fig. 2e–h, S4b & S5d).

The XRD patterns of all catalysts show six peaks at around 19.0° , 31.3° , 36.8° , 44.8° , 59.3° and 65.2° , which are close to the (111), (220),

(311), (400), (331) and (440) facets of spinel Co_3O_4 (PDF#43–1003), respectively (Fig. 2i). The d-spacings of Co_3O_4 (220) and Co_3O_4 (311) in $\text{Co}_3\text{O}_4\text{-Mn}_2$ are consistent with the HRTEM results (Fig. 2c & S4a). Compared with pure Co_3O_4 , we see that there is an obvious peak shift to small diffraction angle when Mn is incorporated, which indicates the increment of lattice. However, there is no obvious peak shift among Mn-incorporated samples with different Mn/Co ratios, indicating that the Mn content in the sample does not increase linearly with the increase of Mn-Co ratio as added in the hydrothermal reaction, which is further confirmed by the XPS and EDX results (Fig. S5). Similarly, the XPS spectra quantify that the Mn-Co ratio in $\text{Co}_3\text{O}_4\text{-Mn}_2$ is about 1:3, consistent with the EDX result (Fig. S4b and S5). After confirming the incorporation of Mn, it is necessary to figure out its status in the spinel Co_3O_4 , which would be helpful to reveal the origin of catalytic performance. However, the XPS spectra of Mn2p and Co2p do not provide any

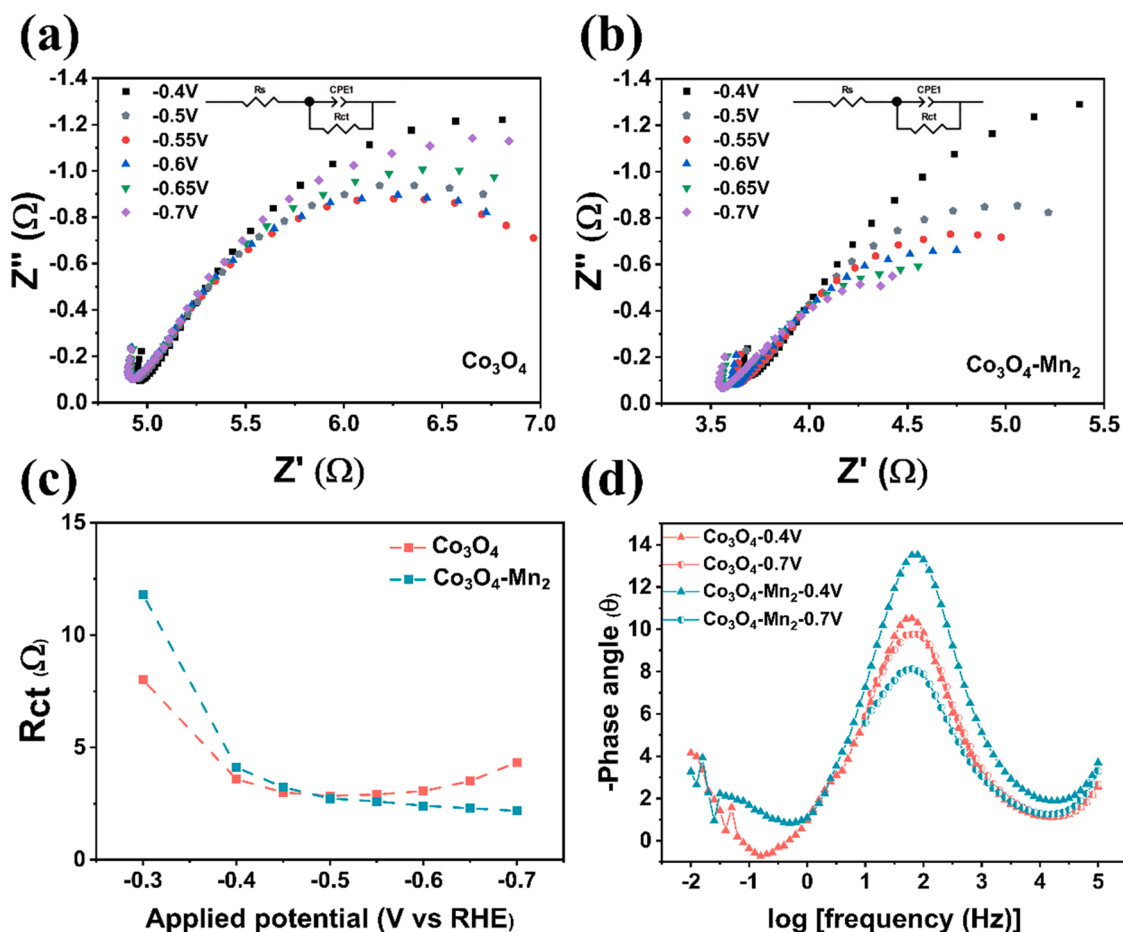


Fig. 4. Nyquist plots for (a) Co_3O_4 and (b) $\text{Co}_3\text{O}_4\text{-Mn}_2$ at different applied potentials vs. RHE in 0.5 M K_2SO_4 + 0.1 M KNO_3 . (c) Response of the total charge transfer resistance (R_{ct}) to the applied potential. (d) Bode phase plots at -0.4 V and -0.7 V vs. RHE in 0.5 M K_2SO_4 + 0.1 M KNO_3 .

evidence for the analysis because there is no obvious peak shift (Figs. S5a & S5b). Therefore, the Raman scattering was used to characterize the surface information of each sample and identify the Mn-incorporation site in Co_3O_4 . For Co_3O_4 , one Raman band at $\sim 191 \text{ cm}^{-1}$ is contributed by the vibration of CoO_4 tetrahedron in Co_3O_4 nanocrystal, and four Raman bands at ~ 510 , 606, 465 and 664 cm^{-1} correspond to the 2F_g , E_g and A_1g Raman-active modes of CoO_6 octahedron (Fig. 2j) [63,68–70]. For the Mn-incorporated Co_3O_4 sample, there is no obvious peak shift of Raman band at 191 cm^{-1} , suggesting that Mn does not incorporate into the CoO_4 tetrahedron. Differently, the Raman signals for the CoO_6 octahedron become broad. Especially, there are two new peaks at 492 and 634 cm^{-1} , which are assigned to the edge-sharing MnO_6 octahedron, indicating that the Mn ion mainly replaces Co of CoO_6 octahedron by forming MnO_6 octahedron. Our DFT results also confirm the results as discussed below. Therefore, we suggest that the surfaces of Mn-incorporated samples are enriched with MnO_6 and CoO_6 octahedrons (Fig. 2j). Meanwhile, the Mn-incorporation could alter the electronic structure of Co_3O_4 , which in turn influences the phonon confinement effect and broaden the Raman bands of CoO_6 octahedrons in the Mn-doped Co_3O_4 samples (Fig. 2j).

3.2. Electrochemical activity

To investigate the electrocatalytic activity of our sample for $\text{e-NO}_3\text{RR}$, a 0.1 M KNO_3 + 0.5 M K_2SO_4 solution was used. Due to the superior FE of pure Co_3O_4 under low potentials, we compared their performances at -1.2 V vs RHE. Among these samples, $\text{Co}_3\text{O}_4\text{-Mn}_2$ exhibits the most superior catalytic activity with the highest ammonia

yield rate of $35 \text{ mg h}^{-1} \text{ cm}^{-2}$ and a FE of 99.5% at -1.2 V vs RHE (Fig. 3a). Compared with the reported transition-metal oxides, $\text{Co}_3\text{O}_4\text{-Mn}_2$ shows the highest ammonia yield and almost 100% FE (Table S1) [46,60,62,63,65–67,71,72]. Additionally, the contamination from the electrolytic setup, electrolytes, and our catalysts is negligible ($0.14 \text{ mg h}^{-1} \text{ cm}^{-2}$) (Fig. S6) [23,46,62]. Furthermore, the isotope labeling experiments under -1 V vs RHE confirm that the ammonia is produced by the reduction of nitrate (Fig. S7). The normalized ammonia yield rates by ECSA show that $\text{Co}_3\text{O}_4\text{-Mn}_2$ exhibits a 2-fold increment compared to Co_3O_4 (Fig. 3a & S8). Although the Co_3O_4 sample has a low onset potential, the fast kinetic process of $\text{Co}_3\text{O}_4\text{-Mn}_2$ results in the low potential when the current density reaches 50 mA/cm^2 or higher, indicating its practical application under high current density (Fig. 3b & 4c). To confirm the activity, the ammonia yield rates, nitrite yield rates, and corresponding FEs of Co_3O_4 and $\text{Co}_3\text{O}_4\text{-Mn}_2$ under different potentials were characterized by performing chronopotentiometry tests (Fig. 3d & S13). Although Co_3O_4 has high selectivity under low potentials (-0.6 ~ -0.8 V), the FE for ammonia decreases when the applied potential is higher than -1 V vs RHE, which limits its practical application. In contrast, the FE of $\text{Co}_3\text{O}_4\text{-Mn}_2$ in $\text{e-NO}_3\text{RR}$ keeps increasing with the increase of applied potential, leading to a high FE of more than 97% as the applied potential is higher than -0.6 V vs RHE (Fig. 3d). The $\text{e-NO}_3\text{RR}$ on $\text{Co}_3\text{O}_4\text{-Mn}_2$ under much higher potentials cannot be done due to the limited mass transportation [5,73]. Thus, combined with fast kinetics, the Mn-incorporation obviously improves the $\text{e-NO}_3\text{RR}$ activity especially under high applied potentials. In addition, the $\text{e-NO}_3\text{RR}$ processes on Co_3O_4 and $\text{Co}_3\text{O}_4\text{-Mn}_2$ under different nitrate concentrations were performed because the diffusion of nitrate from the

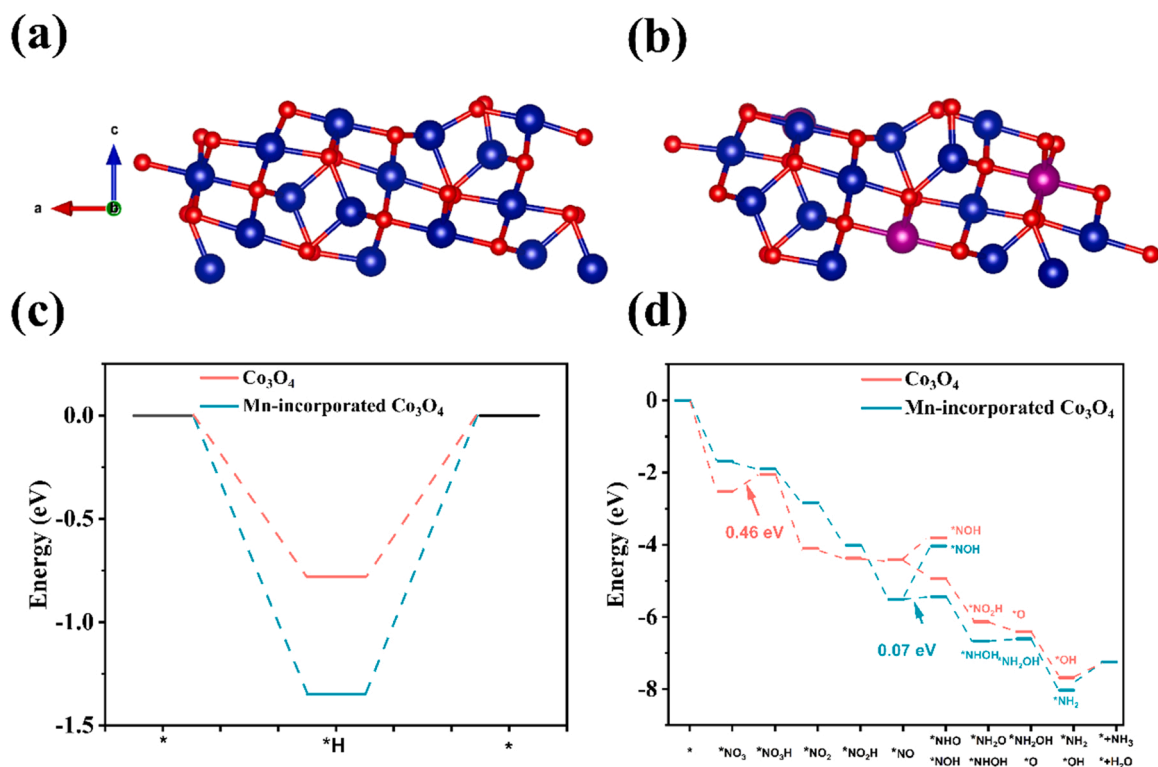


Fig. 5. The side view for (a) Co₃O₄ and (b) Mn-incorporated Co₃O₄ slabs (color notation: dark blue-Co, red-O, and purple-Mn). The energy profiles for e-HER (c) and e-NO₃RR (d) on pure and Mn-incorporated Co₃O₄.

electrolyte to the catalyst surface may play a key role in the reaction rate and competition with e-HER [55,74]. The FE of e-NO₃RR on Co₃O₄ decreases dramatically to about 60% when the nitrate concentration reaches 5 mM due to the competitive e-HER (Fig. 3f), while the selectivity of e-NO₃RR on Co₃O₄-Mn₂ remains a relatively high level with a FE of about 80%, further indicating the improved selectivity. To demonstrate the durability of Co₃O₄-Mn₂, a 10 h stability test by replenishing solution every hour was performed under -1 V vs RHE. It can be observed that the current density keeps increasing as the reaction proceeds and almost recovers to initial state when the solution is refreshed, indicating the good stability (Fig. 3g). The corresponding ammonia yield rate (> 25 mg h⁻¹ cm⁻²) and FE (> 95%) towards ammonia keep almost unchanged, indicating the excellent durability of Co₃O₄-Mn₂ (Fig. 3e & g), which is also in good accordance with the LSV curve and other structural characterization results after the 10 h durability test (Figs. S1, S14 & S15).

EIS is a useful tool to probe the kinetics of electrocatalytic reaction and the property of electrode/electrolyte interface [75]. To identify the origin of improved selectivity, operando EIS measurements were performed. From the LSV curves of Co₃O₄ and Co₃O₄-Mn₂ (Fig. 3b), the e-NO₃RR processes begin at 0 V, while the e-HER processes start at -0.4 V, indicating the possible influence of competitive reaction on the kinetics when the applied potential is higher than -0.4 V. Thus, the Nyquist plots for the e-NO₃RR and e-HER processes were measured from -0.4 ~ -0.7 V in 0.1 M KNO₃ + 0.5 M K₂SO₄, which were fitted with an equivalent circuit and used to describe the adsorption behavior of the reactants (H₂) on the catalyst's surface. Because e-NO₃RR and e-HER share the same reactants, the trends for the changes of R_s , R_{ct} (charge transfer resistance) and R_{cpe} (cpe: constant phase element) may reveal the competition between these two reactions. Comparing with Co₃O₄, Co₃O₄-Mn₂ exhibits lower R_s at different applied potentials, which is in accordance with its fast kinetics (Fig. 4a & 4b) in e-NO₃RR. The EIS spectra of Co₃O₄-Mn₂ show that the diameter of semicircle and corresponding R_{ct} decrease with the increase of applied potential, indicating

the dominant e-NO₃RR progress (Fig. 4b & c). In contrast, the EIS spectra of Co₃O₄ show that the diameter of semicircle decreases initially as the potential increases from -0.4 to -0.55 V, while increases gradually when the applied potential is higher than -0.55 V, indicating the reduced kinetics of e-NO₃RR due to the competitive e-HER, which is in accordance with the gradual increased H₂ FE after -0.6 V (Fig. 4a and S16) [15,76,77]. Additionally, the value of R_{ct} follows the same trend too, which confirms the competition from e-HER (Fig. 4c). At -0.4 V, the phase peak of Co₃O₄-Mn₂ slightly shifts to higher frequency and shows a higher phase angle than that of Co₃O₄, which implies its lower selectivity in e-NO₃RR under low applied potentials (Fig. 4d). Differently, the phase peak of Co₃O₄-Mn₂ in turn exhibits lower phase angle under -0.7 V, indicating improved FE for ammonia and reduced FE for H₂ (Fig. S16) under high applied potentials [51,78,79].

3.3. DFT calculations

To reveal the mechanism, we carried out theoretic calculations based on density-functional theory (DFT). Our DFT study confirms that Mn is easier to replace Co in the CoO₆ octahedrons than that in CoO₄ tetrahedrons because of relatively lower formation energy (Fig. S17), consistent with the Raman results (Fig. 2j). It is found that the lattice fringe distances are well indexed to (220) and (311) planes of Co₃O₄ for both pure Co₃O₄ and Co₃O₄-Mn₂ in the HRTEM images (Fig. 2c, d & S2). As both the (220) and (311) planes are composed of CoO₄ tetrahedrons and CoO₆ octahedrons, the DFT calculations were conducted only on the (311) surface with the termination consisted by 2 Co(Mn)O₄ tetrahedrons and 6 Co(Mn)O₆ octahedrons to investigate the effect of Mn-incorporation on e-HER and e-NO₃RR (Fig. 5a, b & S18). For the e-HER on both surfaces, *H prefers to adsorb on the surface O ion. The Gibbs free energies for the adsorption of *H on Co₃O₄ and Mn-incorporated Co₃O₄ are -0.79 eV and -1.41 eV, respectively, indicating the surface sites on Mn-incorporated Co₃O₄ are less active than those on Co₃O₄ (Fig. 5c). The improved HER activity of Co₃O₄-Mn₂ in

experiment under high potential should be contributed by the improved conductivity (Fig. 3a, Fig. 4). The stronger interaction between *H and surface O ion in the CoO₆ octahedrons induced by the Mn-incorporation is attributed to the weakened Co-O bond. The e-NO₃RR pathways on Co₃O₄ and Mn-incorporated Co₃O₄ surfaces were also studied. There are three e-NO₃RR pathways: NOH pathway from *NO to *NOH (*NOH → *N → *NH → *NH₂ → *NH₃) and two NHO pathway from *NO to *NHO (*NHO → *NHOH → *NH₂OH → *NH₂ → *+NH₃ and *NHO → *NH₂O → NH₃ + *O → *OH → *+H₂O)[80]. The NHO pathway is energetically favorable for both catalysts due to the difficult protonation to *NOH on the NOH pathway. For Co₃O₄, the rate-determining step is *NO₃ → *NO₃H with a ΔG of 0.45 eV (Fig. 5d). Besides, the protonation of *NH₂O leads to the release of NH₃ and leaves *O adsorbed. After incorporating Mn, the most endothermic step changes to *NO → *NHO, which has a much lower ΔG (0.07 eV), in accordance with the above experimental observations. Therefore, the strategy of Mn-incorporation not only suppresses HER by enhancing the interaction with *H, but also promotes e-NO₃RR by changing the reaction pathway and lowering the energy barrier to produce ammonia.

4. Conclusions

In summary, we propose a strategy to improve the catalytic performance of Co₃O₄ for efficient reduction of nitrate to ammonia by incorporating Mn. We find that Mn-incorporated Co₃O₄ nanotubes show a high NH₃ yield of 35 mg h⁻¹ cm⁻² and high FE up to 99.5% at -1.2 V versus RHE under ambient conditions, which outperform most of oxide-based electrocatalysts for e-NO₃RR. The combined experimental and calculational results reveal that the Mn ion can easily replace Co in the CoO₆ octahedron of spinel Co₃O₄ partially, which plays a critical role in suppressing the HER and boosting the e-NO₃RR activity. Our findings may provide an insightful understanding on the catalytic origin and demonstrate that the incorporation is an effective way to engineer the spinel oxides for enhanced activity and selectivity towards the ammonia production in e-NO₃RR.

CRedit authorship contribution statement

Di Liu: Conceptualization, Investigation, Writing – original draft. **Lulu Qiao:** Investigation, Validation, Writing – review & editing. **Yuyun Chen:** Investigation, Validation. **Pengfei Zhou:** Visualization. **Jinxian Feng:** Visualization. **Chon Chio Leong:** Resources. **Kar Wei Ng:** Resources. **Shengjie Peng:** Writing – review & editing. **Shuangpeng Wang:** Funding acquisition, Writing – review & editing. **Weng Fai Ip:** Writing – review & editing. **Hui Pan:** Conceptualization, Funding acquisition, Writing – review & editing.

Declaration of Competing Interest

The authors declare that they have no known competing financial interests or personal relationships that could have appeared to influence the work reported in this paper.

Data availability

Data will be made available on request.

Acknowledgements

This work was supported by the Science and Technology Development Fund (FDCT) from Macau SAR (0081/2019/AMJ, 0154/2019/A3, 0033/2019/AMJ, 0102/2019/A2, and 0111/2022/A2) Multi-Year Research Grants (MYRG2020-00026-FST and MYRG2022-00026-IAPME) from Research & Development Office at University of Macau, and Shenzhen-Hong Kong-Macao Science and Technology Research Programme (Type C) (SGDX20210823103803017) from Shenzhen. The

DFT calculations were performed at the High Performance Computing Cluster (HPCC) of the Information and Communication Technology Office (ICTO) at the University of Macau.

Appendix A. Supporting information

Supplementary data associated with this article can be found in the online version at doi:10.1016/j.apcatb.2022.122293.

References

- [1] C. Smith, A.K. Hill, L. Torrente-Murciano, Current and future role of Haber-Bosch ammonia in a carbon-free energy landscape, *Energy Environ. Sci.* 13 (2020) 331–344.
- [2] R. Jia, Y. Wang, C. Wang, Y. Ling, Y. Yu, B. Zhang, Boosting selective nitrate electroreduction to ammonium by constructing oxygen vacancies in TiO₂, *ACS Catal.* 10 (2020) 3533–3540.
- [3] G.-F. Chen, Y. Yuan, H. Jiang, S.-Y. Ren, L.-X. Ding, L. Ma, T. Wu, J. Lu, H. Wang, Electrochemical reduction of nitrate to ammonia via direct eight-electron transfer using a copper-molecular solid catalyst, *Nat. Energy* 5 (2020) 605–613.
- [4] P.H. van Langevelde, I. Katsounaros, M.T. Koper, Electrocatalytic nitrate reduction for sustainable ammonia production, *Joule* 5 (2021) 290–294.
- [5] J. Li, G. Zhan, J. Yang, F. Quan, C. Mao, Y. Liu, B. Wang, F. Lei, L. Li, A.W. Chan, Efficient ammonia electrosynthesis from nitrate on strained ruthenium nanoclusters, *J. Am. Chem. Soc.* 142 (2020) 7036–7046.
- [6] J. Feng, H. Pan, Electronic state optimization for electrochemical N₂ reduction reaction in aqueous solution, *J. Mater. Chem. A* 8 (2020) 13896–13915.
- [7] V. Kyriakou, I. Garagounis, A. Vourros, E. Vasileiou, M. Stoukides, An electrochemical haber-bosch process, *Joule* 4 (2020) 142–158.
- [8] T. Wu, M.M. Melander, K. Honkala, Coadsorption of NRR and HER intermediates determines the performance of Ru-N₄ toward electrocatalytic N₂ reduction, *ACS Catal.* 12 (2022) 2505–2512.
- [9] K. Chu, Y. Luo, P. Shen, X. Li, Q. Li, Y. Guo, Unveiling the synergy of O-vacancy and heterostructure over MoO_{3-x}/MXene for N₂ electroreduction to NH₃, *Adv. Energy Mater.* 12 (2022), 2103022.
- [10] S.-J. Qian, H. Cao, J.-W. Chen, J.-C. Chen, Y.-G. Wang, J. Li, Critical role of explicit inclusion of solvent and electrode potential in the electrochemical description of nitrogen reduction, *ACS Catal.* 12 (2022) 11530–11540.
- [11] D. Liu, H. Ai, W.T. Lou, F. Li, K.H. Lo, S. Wang, H. Pan, Substrate strain engineering: an efficient strategy to enhance the catalytic activity of SACs on waved graphene for e-NRR, *Sustain. Energy Fuels* 4 (2020) 3773–3779.
- [12] Y. Kong, T. He, A.R. Puente Santiago, D. Liu, A. Du, S. Wang, H. Pan, Unravelling the reaction mechanisms of N₂ fixation on molybdenum nitride: a full DFT study from the pristine surface to heteroatom anchoring, *ChemSusChem* 14 (2021) 3257–3266.
- [13] Y. Luo, Q. Li, Y. Tian, Y. Liu, K. Chu, Amorphization engineered VSe_{2-x} nanosheets with abundant Se-vacancies for enhanced N₂ electroreduction, *J. Mater. Chem. A* 10 (2022) 1742–1749.
- [14] Q. Chen, J. Liang, Q. Liu, K. Dong, L. Yue, P. Wei, Y. Luo, Q. Liu, N. Li, B. Tang, A. A. Alshehri, M. Hamdy, Z. Jiang, X. Sun, Co nanoparticle-decorated pomelo-peel-derived carbon enabled high-efficiency electrocatalytic nitrate reduction to ammonia, *Chem. Commun.* 58 (2022) 4259–4262.
- [15] X. Zhu, S. Mou, Q. Peng, Q. Liu, Y. Luo, G. Chen, S. Gao, X. Sun, Aqueous electrocatalytic N₂ reduction for ambient NH₃ synthesis: recent advances in catalyst development and performance improvement, *J. Mater. Chem. A* 8 (2020) 1545–1556.
- [16] H. Wang, H. Yu, Z. Wang, Y. Li, Y. Xu, X. Li, H. Xue, L. Wang, Electrochemical fabrication of porous Au film on Ni foam for nitrogen reduction to ammonia, *Small* 15 (2019), 1804769.
- [17] P. Shen, X. Li, Y. Luo, N. Zhang, X. Zhao, K. Chu, Ultra-efficient N₂ electroreduction achieved over a rhodium single-atom catalyst (Rh₁/MnO₂) in water-in-salt electrolyte, *Appl. Catal. B Environ.* 316 (2022), 121651.
- [18] Y. Kong, L. Wu, X. Yang, Y. Li, S. Zheng, B. Yang, Z. Li, Q. Zhang, S. Zhou, L. Lei, Accelerating protonation kinetics for ammonia electrosynthesis on single iron sites embedded in carbon with intrinsic defects, *Adv. Funct. Mater.* (2022), 2205409.
- [19] Y. Sun, Y. Han, X. Zhang, W. Cai, Y. Zhang, Y. Zhang, Z. Li, B. Li, J. Lai, L. Wang, TiO_{1.8} with lattice H for effective electrocatalytic nitrogen fixation, *Appl. Catal. B: Environ.* (2022), 121933.
- [20] D. Liu, M. Chen, X. Du, H. Ai, K.H. Lo, S. Wang, S. Chen, G. Xing, X. Wang, H. Pan, Development of electrocatalysts for efficient nitrogen reduction reaction under ambient condition, *Adv. Funct. Mater.* 31 (2021), 2008983.
- [21] H. Chen, J. Liang, K. Dong, L. Yue, T. Li, Y. Luo, Z. Feng, N. Li, M.S. Hamdy, A. A. Alshehri, Y. Wang, X. Sun, Q. Liu, Ambient electrochemical N₂-to-NH₃ conversion catalyzed by TiO₂ decorated Juncus effusus-derived carbon microtubes, *Inorg. Chem. Front.* 9 (2022) 1514–1519.
- [22] Y. Luo, P. Shen, X. Li, Y. Guo, K. Chu, Sulfur-deficient Bi₂S_{3-x} synergistically coupling Ti₃C₂T_x-MXene for boosting electrocatalytic N₂ reduction, *Nano Res.* 15 (2022) 3991–3999.
- [23] S. Li, Y. Wang, J. Liang, T. Xu, D. Ma, Q. Liu, T. Li, S. Xu, G. Chen, A.M. Asiri, Y. Luo, Q. Wu, X. Sun, TiB₂ thin film enabled efficient NH₃ electrosynthesis at ambient conditions, *Mater. Today Phys.* 18 (2021), 100396.

- [24] L. Zhang, X. Ji, X. Ren, Y. Ma, X. Shi, Z. Tian, A.M. Asiri, L. Chen, B. Tang, X. Sun, Electrochemical ammonia synthesis via nitrogen reduction reaction on a MoS₂ catalyst: theoretical and experimental studies, *Adv. Mater.* 30 (2018), 1800191.
- [25] H. Liu, J. Park, Y. Chen, Y. Qiu, Y. Cheng, K. Srivastava, S. Gu, B.H. Shanks, L. T. Rolling, W. Li, Electrocatalytic nitrate reduction on oxide-derived silver with tunable selectivity to nitrite and ammonia, *ACS Catal.* 11 (2021) 8431–8442.
- [26] Y. Zhao, Y. Liu, Z. Zhang, Z. Mo, C. Wang, S. Gao, Flower-like open-structured polycrystalline copper with synergistic multi-crystal plane for efficient electrocatalytic reduction of nitrate to ammonia, *Nano Energy* 97 (2022), 107124.
- [27] X. Zhang, Y. Wang, C. Liu, Y. Yu, S. Lu, B. Zhang, Recent advances in non-noble metal electrocatalysts for nitrate reduction, *Chem. Eng. J.* 403 (2021), 126269.
- [28] Q. Hu, Y. Qin, X. Wang, Z. Wang, X. Huang, H. Zheng, K. Gao, H. Yang, P. Zhang, M. Shao, Reaction intermediate-mediated electrocatalyst synthesis favors specified facet and defect exposure for efficient nitrate–ammonia conversion, *Energy Environ. Sci.* 14 (2021) 4989–4997.
- [29] Z.-Y. Wu, M. Karamad, X. Yong, Q. Huang, D.A. Cullen, P. Zhu, C. Xia, Q. Xiao, M. Shakouri, F.-Y. Chen, Electrochemical ammonia synthesis via nitrate reduction on Fe single atom catalyst, *Nat. Commun.* 12 (2021) 1–10.
- [30] S. Garcia-Segura, M. Lanzarini-Lopes, K. Hristovski, P. Westerhoff, Electrocatalytic reduction of nitrate: fundamentals to full-scale water treatment applications, *Appl. Catal. B: Environ.* 236 (2018) 546–568.
- [31] H. Xu, Y. Ma, J. Chen, W.-x. Zhang, J. Yang, Electrocatalytic reduction of nitrate—a step towards a sustainable nitrogen cycle, *Chem. Soc. Rev.* (2022).
- [32] W. Duan, G. Li, Z. Lei, T. Zhu, Y. Xue, C. Wei, C. Feng, Highly active and durable carbon electrocatalyst for nitrate reduction reaction, *Water Res.* 161 (2019) 126–135.
- [33] Y.-J. Shih, Z.-L. Wu, Electroplating of surfactant-modified tin catalyst over a nickel foam electrode (Sn/Ni) for selective N₂ yield from nitrate reduction as affected by Sn (200) and Sn (101) crystal facets, *Appl. Catal. B Environ.* 285 (2021), 119784.
- [34] Y. Yao, S. Zhu, H. Wang, H. Li, M. Shao, A spectroscopic study of electrochemical nitrogen and nitrate reduction on rhodium surfaces, *Angew. Chem.* 132 (2020) 10565–10569.
- [35] W. Teng, N. Bai, Y. Liu, Y. Liu, J. Fan, W.-x. Zhang, Selective nitrate reduction to dinitrogen by electrocatalysis on nanoscale iron encapsulated in mesoporous carbon, *Environ. Sci. Technol.* 52 (2018) 230–236.
- [36] J.F. Su, W.-F. Kuan, C.-L. Chen, C.-P. Huang, Enhancing electrochemical nitrate reduction toward dinitrogen selectivity on Sn-Pd bimetallic electrodes by surface structure design, *Appl. Catal. A Gen* 606 (2020), 117809.
- [37] Y. Yao, L. Zhao, J. Dai, J. Wang, C. Fang, G. Zhan, Q. Zheng, W. Hou, L. Zhang, Single atom Ru monolithic electrode for efficient chlorine evolution and nitrate reduction, *Angew. Chem. Int. Ed.* 61 (2022), e202208215.
- [38] Z. Wang, S.D. Young, B.R. Goldsmith, N. Singh, Increasing electrocatalytic nitrate reduction activity by controlling adsorption through PtRu alloying, *J. Catal.* 395 (2021) 143–154.
- [39] Y. Wang, C. Wang, M. Li, Y. Yu, B. Zhang, Nitrate electroreduction: mechanism insight, in situ characterization, performance evaluation, and challenges, *Chem. Soc. Rev.* 50 (2021) 6720–6733.
- [40] Z. Gong, W. Zhong, Z. He, C. Jia, D. Zhou, N. Zhang, X. Kang, Y. Chen, Improving electrochemical nitrate reduction activity of layered perovskite oxide La₂CuO₄ via B-site doping, *Catal. Today* (2022).
- [41] Y. Lan, J. Chen, H. Zhang, W.-x. Zhang, J. Yang, Fe/Fe₃C nanoparticle-decorated N-doped carbon nanofibers for improving the nitrogen selectivity of electrocatalytic nitrate reduction, *J. Mater. Chem. A* 8 (2020) 15853–15863.
- [42] T. Hu, M. Wang, C. Guo, C.M. Li, Functionalized MXenes for efficient electrocatalytic nitrate reduction to ammonia, *J. Mater. Chem. A* 10 (2022) 8923–8931.
- [43] Z.A. Jonoush, A. Rezaee, A. Ghaffarinejad, Electrocatalytic nitrate reduction using Fe₀/Fe₃O₄ nanoparticles immobilized on nickel foam: selectivity and energy consumption studies, *J. Clean. Prod.* 242 (2020), 118569.
- [44] Q.-L. Hong, J. Zhou, Q.-G. Zhai, Y.-C. Jiang, M.-C. Hu, X. Xiao, S.-N. Li, Y. Chen, Cobalt phosphide nanorings towards efficient electrocatalytic nitrate reduction to ammonia, *Chem. Commun.* 57 (2021) 11621–11624.
- [45] Y. Xu, Y. Wen, T. Ren, H. Yu, K. Deng, Z. Wang, X. Li, L. Wang, H. Wang, Engineering the surface chemical microenvironment over CuO nanowire arrays by polyaniline modification for efficient ammonia electrosynthesis from nitrate, *Appl. Catal. B Environ.* 320 (2023), 121981.
- [46] T. Ren, Z. Yu, H. Yu, K. Deng, Z. Wang, X. Li, H. Wang, L. Wang, Y. Xu, Interfacial polarization in metal-organic framework reconstructed Cu/Pd/CuO_x multi-phase heterostructures for electrocatalytic nitrate reduction to ammonia, *Appl. Catal. B Environ.* 318 (2022), 121805.
- [47] T. Mou, J. Liang, Z. Ma, L. Zhang, Y. Lin, T. Li, Q. Liu, Y. Luo, Y. Liu, S. Gao, H. Zhao, A.M. Asiri, D. Ma, X. Sun, High-efficiency electrohydrogenation of nitric oxide to ammonia on a Ni₂P nanowire array under ambient conditions, *J. Mater. Chem. A* 9 (2021) 24268–24275.
- [48] X. He, X. Li, X. Fan, J. Li, D. Zhao, L. Zhang, S. Sun, Y. Luo, D. Zheng, L. Xie, A. M. Asiri, Q. Liu, X. Sun, Ambient electroreduction of nitrite to ammonia over Ni nanoparticle supported on molasses-derived carbon sheets, *ACS Appl. Nano Mater.* (2022).
- [49] D. Zhao, J. Liang, J. Li, L. Zhang, K. Dong, L. Yue, Y. Luo, Y. Ren, Q. Liu, M. S. Hamdy, Q. Li, Q. Kong, X. Sun, A TiO₂-x nanobelt array with oxygen vacancies: an efficient electrocatalyst toward nitrite conversion to ammonia, *Chem. Commun.* 58 (2022) 3669–3672.
- [50] P. Liu, J. Liang, J. Wang, L. Zhang, J. Li, L. Yue, Y. Ren, T. Li, Y. Luo, N. Li, B. Tang, Q. Liu, A.M. Asiri, Q. Kong, X. Sun, High-performance NH₃ production via NO electroreduction over a NiO nanosheet array, *Chem. Commun.* 57 (2021) 13562–13565.
- [51] J. Liang, P. Liu, Q. Li, T. Li, L. Yue, Y. Luo, Q. Liu, N. Li, B. Tang, A.A. Alshehri, I. Shakir, P.O. Agboola, C. Sun, X. Sun, Amorphous boron carbide on titanium dioxide nanobelt arrays for high-efficiency electrocatalytic NO reduction to NH₃, *Angew. Chem. Int. Ed.* 61 (2022), e202202087.
- [52] Z. Wang, Z. Dai, S. Wang, H. Zhang, W. Tian, Y. Xu, X. Li, L. Wang, H. Wang, Enhancing electrochemical ammonia synthesis on palladium nanorods through surface hydrogenation, *Chem. Eng. J.* 416 (2021), 129105.
- [53] J. Chen, T. Gong, Q. Hou, J. Li, L. Zhang, D. Zhao, Y. Luo, D. Zheng, T. Li, S. Sun, Z. Cai, Q. Liu, L. Xie, M. Wu, A.A. Alshehri, X. Sun, Co/N-doped carbon nanosphere derived from adenine-based metal organic framework enabled high-efficiency electrocatalytic nitrate reduction to ammonia, *Chem. Commun.* (2022).
- [54] P. Shen, G. Wang, K. Chen, J. Kang, D. Ma, K. Chu, Selenium-vacancy-rich WSe₂ for nitrate electroreduction to ammonia, *J. Colloid Interface Sci.* 629 (2023) 563–570.
- [55] J. Wang, C. Cai, Y. Wang, X. Yang, D. Wu, Y. Zhu, M. Li, M. Gu, M. Shao, Electrocatalytic reduction of nitrate to ammonia on low-cost ultrathin CoO_x nanosheets, *ACS Catal.* 11 (2021) 15135–15140.
- [56] Z. Niu, S. Fan, X. Li, P. Wang, Z. Liu, J. Wang, C. Bai, D. Zhang, Bifunctional copper-cobalt spinel electrocatalysts for efficient tandem-like nitrate reduction to ammonia, *Chem. Eng. J.* 450 (2022), 138343.
- [57] W. Deelod, T. Priamushko, J. Čížek, S. Suramitr, F. Kleitz, Defect-engineered hydroxylated mesoporous spinel oxides as bifunctional electrocatalysts for oxygen reduction and evolution reactions, *ACS Appl. Mater. Interfaces* (2022).
- [58] C. Mu, J. Mao, J. Guo, Q. Guo, Z. Li, W. Qin, Z. Hu, K. Davey, T. Ling, S.Z. Qiao, Rational design of spinel cobalt vanadate oxide Co₂VO₄ for superior electrocatalysis, *Adv. Mater.* 32 (2020), 1907168.
- [59] J. Shan, C. Ye, S. Chen, T. Sun, Y. Jiao, L. Liu, C. Zhu, L. Song, Y. Han, M. Jaroniec, Short-range ordered iridium single atoms integrated into cobalt oxide spinel structure for highly efficient electrocatalytic water oxidation, *J. Am. Chem. Soc.* 143 (2021) 5201–5211.
- [60] P. Wei, J. Liang, Q. Liu, L. Xie, X. Tong, Y. Ren, T. Li, Y. Luo, N. Li, B. Tang, A. M. Asiri, M.S. Hamdy, Q. Kong, Z. Wang, X. Sun, Iron-doped cobalt oxide nanowire array for efficient electrocatalytic nitrate-to-ammonia conversion, *J. Colloid Interface Sci.* 615 (2022) 636–642.
- [61] Q. Liu, L. Xie, J. Liang, Y. Ren, Y. Wang, L. Zhang, L. Yue, T. Li, Y. Luo, N. Li, B. Tang, Y. Liu, S. Gao, A.A. Alshehri, I. Shakir, P.O. Agboola, Q. Kong, Q. Wang, D. Ma, X. Sun, Ambient ammonia synthesis via electrochemical reduction of nitrate enabled by NiCo₂O₄ nanowire array, *Small* 18 (2022), 2106961.
- [62] X. Xu, L. Hu, Z. Li, L. Xie, S. Sun, L. Zhang, J. Li, Y. Luo, X. Yan, M.S. Hamdy, Q. Kong, X. Sun, Q. Liu, Oxygen vacancies in Co₃O₄ nanowires promote nitrate electroreduction for ammonia synthesis, *Sustain. Energy Fuels* 6 (2022) 4130–4136.
- [63] Z. Deng, C. Ma, Z. Li, Y. Luo, L. Zhang, S. Sun, Q. Liu, J. Du, Q. Lu, B. Zheng, X. Sun, High-efficiency electrochemical nitrate reduction to ammonia on a Co₃O₄ nanowire array catalyst with cobalt vacancies, *ACS Appl. Mater. Interfaces* (2022).
- [64] X. Fan, C. Ma, D. Zhao, Z. Deng, L. Zhang, Y. Wang, Y. Luo, D. Zheng, T. Li, J. Zhang, S. Sun, Q. Lu, X. Sun, Unveiling selective nitrate reduction to ammonia with Co₃O₄ nanosheets/TiO₂ nanobelt heterostructure catalyst, *J. Colloid Interface Sci.* (2022).
- [65] J. Li, D. Zhao, L. Zhang, Y. Ren, L. Yue, Z. Li, S. Sun, Y. Luo, Q. Chen, T. Li, K. Dong, Q. Liu, Q. Kong, X. Sun, Boosting electrochemical nitrate-to-ammonia conversion by self-supported MnCo₂O₄ nanowire array, *J. Colloid Interface Sci.* 629 (2023) 805–812.
- [66] J. Li, D. Zhao, L. Zhang, L. Yue, Y. Luo, Q. Liu, N. Li, A.A. Alshehri, M.S. Hamdy, Q. Li, X. Sun, A FeCo₂O₄ nanowire array enabled electrochemical nitrate conversion to ammonia, *Chem. Commun.* 58 (2022) 4480–4483.
- [67] Z. Li, J. Liang, Q. Liu, L. Xie, L. Zhang, Y. Ren, L. Yue, N. Li, B. Tang, A.A. Alshehri, M.S. Hamdy, Y. Luo, Q. Kong, X. Sun, High-efficiency ammonia electrosynthesis via selective reduction of nitrate on ZnCo₂O₄ nanosheet array, *Mater. Today Phys.* 23 (2022), 100619.
- [68] S. Mo, Q. Zhang, Y. Sun, M. Zhang, J. Li, Q. Ren, M. Fu, J. Wu, L. Chen, D. Ye, Gaseous CO and toluene co-oxidation over monolithic core-shell Co₃O₄-based hetero-structured catalysts, *J. Mater. Chem. A* 7 (2019) 16197–16210.
- [69] Z. Cao, W. Wang, H. Ma, L. Xiao, J. Li, Y. Sun, J. Sheng, F. Dong, Porous Mn-doped Co₃O₄ nanosheets: Gas sensing performance and interfacial mechanism investigation with in situ DRIFTS, *Sens. Actuators B Chem.* 353 (2022), 131155.
- [70] J. Zhong, Y. Zeng, M. Zhang, W. Feng, D. Xiao, J. Wu, P. Chen, M. Fu, D. Ye, Toluene oxidation process and proper mechanism over Co₃O₄ nanotubes: Investigation through in-situ DRIFTS combined with PTR-TOF-MS and quasi in-situ XPS, *Chem. Eng. J.* 397 (2020), 125375.
- [71] Q. Liu, L. Xie, J. Liang, Y. Ren, Y. Wang, L. Zhang, L. Yue, T. Li, Y. Luo, N. Li, B. Tang, Y. Liu, S. Gao, A.A. Alshehri, I. Shakir, P.O. Agboola, Q. Kong, Q. Wang, D. Ma, X. Sun, Ambient ammonia synthesis via electrochemical reduction of nitrate enabled by NiCo₂O₄ nanowire array, *Small* 18 (2022), 2106961.
- [72] Z. Niu, S. Fan, X. Li, J. Duan, A. Chen, Interfacial engineering of CoMn₂O₄/NC induced electronic delocalization boosts electrocatalytic nitrogen oxyanions reduction to ammonia, *Appl. Catal. B Environ.* 322 (2023), 122090.
- [73] X. Fan, J. Liang, L. Zhang, D. Zhao, L. Yue, Y. Luo, Q. Liu, L. Xie, N. Li, B. Tang, Q. Kong, X. Sun, Enhanced electrocatalytic nitrate reduction to ammonia using plasma-induced oxygen vacancies in CoTiO₃-x nanofiber, *Carbon Neutralization* 1 (2022) 6–13.
- [74] J. Liang, Q. Liu, A.A. Alshehri, X. Sun, Recent advances in nanostructured heterogeneous catalysts for N-cycle electrocatalysis, *Nano Res. Energy* 1 (2022), e9120010.
- [75] Z. Xiao, Y.-C. Huang, C.-L. Dong, C. Xie, Z. Liu, S. Du, W. Chen, D. Yan, L. Tao, Z. Shu, G. Zhang, H. Duan, Y. Wang, Y. Zou, R. Chen, S. Wang, Operando

- identification of the dynamic behavior of oxygen vacancy-rich Co_3O_4 for oxygen evolution reaction, *J. Am. Chem. Soc.* 142 (2020) 12087–12095.
- [76] W. Chen, L. Xu, X. Zhu, Y.-C. Huang, W. Zhou, D. Wang, Y. Zhou, S. Du, Q. Li, C. Xie, L. Tao, C.-L. Dong, J. Liu, Y. Wang, R. Chen, H. Su, C. Chen, Y. Zou, Y. Li, Q. Liu, S. Wang, Unveiling the electrooxidation of urea: intramolecular coupling of the N–N bond, *Angew. Chem. Int. Ed.* 60 (2021) 7297–7307.
- [77] Q. Liu, T. Xu, Y. Luo, Q. Kong, T. Li, S. Lu, A.A. Alshehri, K.A. Alzahrani, X. Sun, Recent advances in strategies for highly selective electrocatalytic N_2 reduction toward ambient NH_3 synthesis, *Curr. Opin. Electrochem.* 29 (2021), 100766.
- [78] L. Zhang, J. Liang, Y. Wang, T. Mou, Y. Lin, L. Yue, T. Li, Q. Liu, Y. Luo, N. Li, B. Tang, Y. Liu, S. Gao, A.A. Alshehri, X. Guo, D. Ma, X. Sun, High-performance electrochemical NO reduction into NH_3 by MoS_2 nanosheet, *Angew. Chem.* 133 (2021) 25467–25472.
- [79] H.-j. Chen, Z.-q. Xu, S. Sun, Y. Luo, Q. Liu, M.S. Hamdy, Z.-s. Feng, X. Sun, Y. Wang, Plasma-etched Ti_2O_3 with oxygen vacancies for enhanced NH_3 electrosynthesis and Zn– N_2 batteries, *Inorg. Chem. Front.* 9 (2022) 4608–4613.
- [80] S. Ye, Z. Chen, G. Zhang, W. Chen, C. Peng, X. Yang, L. Zheng, Y. Li, X. Ren, H. Cao, D. Xue, J. Qiu, Q. Zhang, J. Liu, Elucidating the activity, mechanism and application of selective electrosynthesis of ammonia from nitrate on cobalt phosphide, *Energy Environ. Sci.* 15 (2022) 760–770.